Journal of
Materials Chemistry A

Materials for energy and sustainability

rsc.li/materials-a

ROYAL SOCIETY
OF **CHEMISTRY**
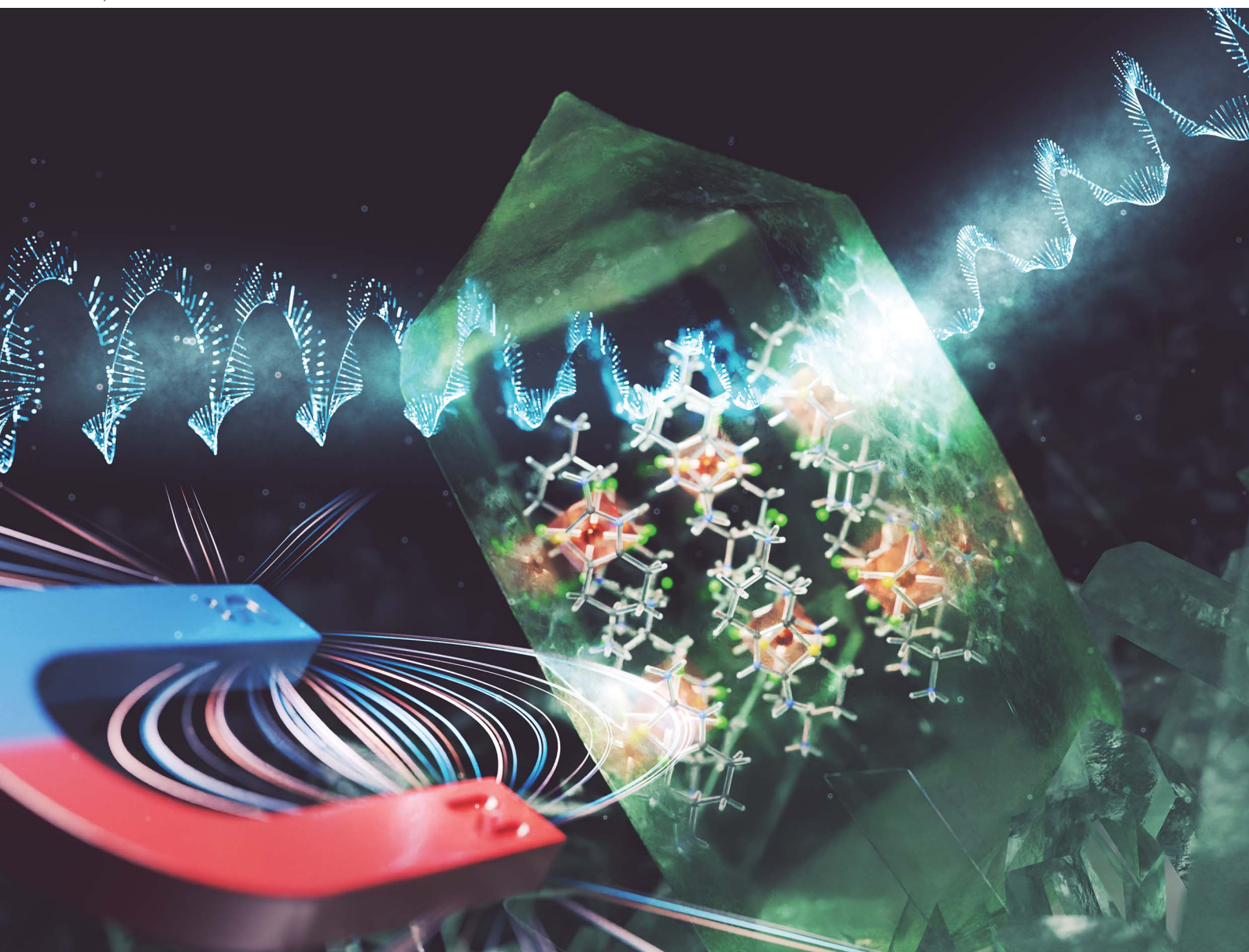
PAPER
Ioannis Spanopoulos *et al.*
Synthesis, optical, electronic and magnetic studies of
air-stable chiral Cu(II) chlorides

PAPER

Check for updates

Synthesis, optical, electronic and magnetic studies of air-stable chiral Cu(II) chlorides†

Ali Azmy,[a] Nivarthana W. Y. A. Y. Mudiyanselage,[b] Kamal E. S. Nassar,[a] Mike Pham,[a] Nourdine Zibouche, [c] Manh-Huong Phan [b] and Ioannis Spanopoulos [*a]

Chiral magnetic metal halide semiconductors (MHSs) have recently emerged as a unique platform of hybrid materials for state-of-the-art applications, where both chiroptical and magnetic properties are essential. Motivated by the scarcity of MHS compounds that feature the latter traits and the absence of relevant structure–property relationships, we present here the synthesis and the optical, electronic, and magnetic properties of two new polar 0D, Cu(II) based materials, namely $(S-/R-THBTD)_2CuCl_6$, where THBTD = 4,5,6,7-tetrahydro-benzothiazole-2,6-diamine. Both enantiomers exhibit direct and indirect optical bandgap characteristics based on UV-vis and density functional theory (DFT) calculations, while circular dichroism (CD) measurements confirmed their chiral character. Magnetometry measurements revealed a notable transition from a paramagnetic to a ferromagnetic-like state at around 4 K, with a low-temperature saturation magnetization value of up to 9.86 emu g^{-1}, which is among the highest reported for chiral magnetic MHSs. Notably, $(S-/R-THBTD)_2CuCl_6$ maintain their structural integrity and magnetic and optical properties (based on UV-vis studies) after one year of air exposure, a record stability performance among chiral magnetic MHSs. This work proves that air-stable MHSs with competitive chiroptical and magnetic properties can be acquired by properly selecting suitable templating agents, paving the way for further materials development.

Introduction

Chiral materials are the basis of chiral photonics and are exploited in various applications, including quantum communication,[1] spin-based transistors,[2] spin valves,[3] magnetic random-access memory (MRAM),[4] and photonic artificial synapses (PAS).[5] Their performance is ascribed to a unique combination of attributes, including circular dichroism (CD),

aDepartment of Chemistry, University of South Florida, Tampa, Florida 33620, USA. E-mail: spanopoulos@usf.edu

bDepartment of Physics, University of South Florida, Tampa, Florida 33620, USA

cDepartment of Chemistry, University of Lancaster, Lancaster, LA1 4YW, UK

Ioannis Spanopoulos acquired his PhD in Materials Chemistry from the University of Crete, working on metal–organic frameworks for gas storage and separation applications. He then joined the research group of Prof. Mercouri G. Kanatzidis at Northwestern University as a post-doctoral fellow, developing perovskite semiconductors for optoelectronic applications. In 2021, he started his independent career at the University of South Florida as an Assistant Professor in the Departments of Chemistry and Chemical, Biological and Materials Engineering. He received the 2020 IIN Outstanding Researcher Award from the International Institute for Nanotechnology, and the 2022 ACS PRF Doctoral New Investigator Research Award. He is a Fellow of the International Association of Advanced Materials (IAAM) and a Highly Cited Researcher for the Year 2022. Research at the Spanopoulos Group focuses on utilizing molecular and crystal engineering to design and synthesize next-generation, multi-functional materials for energy and environment-related applications. The group recently reported two new families of materials, Porous Metal Halide Semiconductors (PMHSs) and crystalline Fullerene-based Metal Halide Semiconductors (FMHSs).

Ioannis Spanopoulos

25730 | *J. Mater. Chem. A*, 2024, **12**, 25730–25739

This journal is © The Royal Society of Chemistry 2024

circularly polarized photoluminescence (CPL), nonlinear optical (NLO) properties, and the bulk photovoltaic effect (BPVE).[6–8] Combining chirality and magnetism within the same material gives access to more intricate applications, such as spin–orbit torque memory devices[9] and magneto-optical modulators.[10] Therefore, the development of chiral magnetic semiconductor materials is greatly sought after.

To this end, hybrid (organic–inorganic) metal halide semiconductors (MHSs) represent a versatile solution for the aforementioned demanding applications. Evidently, by means of molecular and crystal engineering, it is possible not only to introduce chirality and magnetism within the same crystal structure but also to fine-tune the corresponding optoelectronic and magnetic properties. Furthermore, MHSs feature a plethora of traits, such as long spin lifetimes,[7] long diffusion lengths,[11] high carrier mobility,[12] strong spin–orbit coupling (SOC),[13] and large Rashba/Dresselhaus (R/D) splitting,[14,15] which are difficult to be encountered altogether in other classes of fully organic or inorganic semiconductors.

Incorporating chirality into MHSs can generally be achieved by utilizing chiral organic molecules as counter cations and structure-directing agents, giving rise to non-centrosymmetric structural motifs.[16] Moreover, their hybrid nature allows the use of transition-metal ions, such as Cr(II), Cu(II), Mn(II), Fe(II), Co(II), and Ni(II), thus promoting the acquisition of chiral, polar ferromagnetic or ferroelectric MHSs.[17–19]

Despite the exquisite properties of chiral magnetic transition metal halides, there are a limited number of materials reported, evaluating both their magnetic and chiro-optical properties. In particular, in 2020 Sun *et al.* reported two copper-based metal halides, namely $(R\text{-MPEA})_2CuCl_4$ and $(S\text{-MPEA})_2CuCl_4$ $(R\text{-}/S\text{-}$ MPEA $= R\text{-}/S\text{-}(+)\text{-}\beta\text{-methylphenethylammonium})$, revealing strong magneto-chiral anisotropy,[20] Xue *et al.* reported a new layered chiral iron double perovskite with magnetic ordering with the formula $(R\text{-MPA})_4AgFeCl_8$, where $R\text{-MPA}$ is $R\text{-}(+)\text{-}\beta\text{-}$ methylphenethylammonium[21] and Panda *et al.* reported two manganese halides based on 1,4-diazabicyclo[2.2.2]octane (DABCO) with the formula $(H_2DABCO)MnX_4\cdot4H_2O$ (X = Cl and Br) that crystallized in the $P2_12_12_1$ space group and exhibited the magnetocaloric effect at low temperatures.[22] In 2021, Taniguchi *et al.* evaluated the magnetoelectric effect in $(R\text{-}/S\text{-}$ MPA)$_2CuCl_4$,[17] while in 2022, they developed two chiral manganese chloride enantiomers $[R\text{-}/S\text{-MPA}]_2[MnCl_4(H_2O)]$ featuring weak ferromagnetic properties.[23] Ai *et al.* synthesized a 2D Cr^{2+}-based compound, namely $([DFCBA]_2CrCl_4]$, (DFCBA = 3,3-difluoro-ocyclobutyslammonium), which exhibited both ferroelectricity and ferromagnetism,[24] while Lu *et al.* shed light on the chiroptical and magnetic properties of $(R\text{-}/S\text{-MBA})_3Ru_2$-Br$_9$ (MBA = methylbenzylammonium).[18]

On the road to device assembly and commercialization,[25] the long-term environmental stability of chiral magnetic MHSs is crucial and must be evaluated. Although there are multiple reports on the air stability of chiral lead-free MHSs,[26] there is almost a complete absence of information on the air stability of chiral magnetic MHSs.

Motivated by the above concerns, we report here the synthesis and chiro-optical and magnetic properties of two new

0D Cu(II) chloride compounds, namely $(S\text{-}/R\text{-THBTD})_2CuCl_6$ (THBTD = 4,5,6,7-tetrahydro-benzothiazole-2,6-diamine), which have been air stable for a year so far. Both compounds crystallize in the triclinic space group $P1$, diffuse reflectance CD (DRCD) verified the chiral nature of the two structures, while magnetic studies revealed a transition from the paramagnetic to a ferromagnetic-like state at ~4 K, with a low-temperature saturation magnetization value of up to 9.86 emu g^{-1}, among the highest reported for chiral magnetic MHSs.

Results and discussion

Synthetic aspects and structural characterization

Green block crystals of $(S\text{-}/R\text{-THBTD})_2CuCl_6$ (R or S) were acquired through the reaction of copper(II) chloride with the chiral ligand in a hot HCl solution. When the concentration of the organic linker varies from 0.25 M to 0.1 M, the size of the crystals can be tuned from 30 μm to 0.3 cm (Fig. S1†). Scanning electron microscopy (SEM) studies revealed the formation of well-faceted block crystals, while energy dispersive spectroscopy (EDS) measurements confirmed the atomic ratio between Cu and Cl to be 1 : 6, consistent with the proposed formula (Fig. S2†).

Single crystal XRD studies demonstrate that both enantiomers are isostructural, crystalizing in the polar triclinic space group $P1$ (Table 1). The structure consists of isolated square-planar $[CuCl_4]^{2-}$ moieties separated and charge-balanced by two Cl$^-$ and two double protonated THBTD ligands (Fig. 1a and b). Under current synthetic conditions only two of the three amine groups are protonated, the aliphatic primary amine (R–NH$_3$) and the aromatic secondary amine (–NH=). The corresponding chiral organic cations feature an antiparallel brick-wall configuration and are eclipsed along the c-axis, lying at a distance of 3.2 and 3.6 Å along the c and b-axes, respectively.

Having a closer look at the R analog, we observe that the corresponding Cu–Cl bond length ranges between 2.245(3) and 2.272(2) Å (Table S3† and Fig. 1c). It is pointed out that these Cu(II)–Cl bond lengths are consistent with previously reported 0D Cu(II) chlorides, such as $(R\text{-}/S\text{-MBA})_2CuCl_4$ with values ranging from 2.234 to 2.262 Å, $(R\text{-}/S\text{-NEA})_2CuCl_4$ (NEA = α-naphthylethylamine) featuring bond lengths spanning from 2.2380 to 2.2592 Å and $(R\text{-}/S\text{-})\text{-}(FE)_2CuCl_4$ (FE=(4-fluorophenyl) ethylamine) exhibiting Cu–Cl values varying from 2.240 to 2.267 Å, albeit at 100 K.[27–30] There is a miniscule asymmetric distortion in $[CuCl_4]^{2-}$ deriving from the deviation of Cl–Cu–Cl angles from the ideal value of 90° for square planar moieties. Two of the corresponding bond angles lie slightly below the latter value (89.02° and 89.97°), while the other two angles lie above it (90.25° and 91.06°) (Table S4†).

Interestingly, the coordination environment of Cu(II) in $(S\text{-}/R\text{-}$ THBTD)$_2CuCl_6$ is quite uncommon for 0D Cu(II) halides, featuring usually a tetrahedral geometry, as in the case of $(R/S)\text{-}$ (MBA)$_2CuCl_4$.[31] Apparently, for $(R\text{-THBTD})_2CuCl_6$ in particular, the number and magnitude of hydrogen bonds in-plane strongly impose a square planar coordination geometry. There are multiple interactions among the hydrogen atoms of the three amine groups of the ligand, the aliphatic primary amine

This journal is © The Royal Society of Chemistry 2024

J. Mater. Chem. A, 2024, **12**, 25730–25739 | **25731**

Table 1 Crystal and structure refinement data for $(R\text{-}/S\text{-THBTD})_2CuCl_6$ at various temperatures[a]

Compound	$(R\text{-THBTD})_2CuCl_6$ at 296 K	$(S\text{-THBTD})_2CuCl_6$ at 296 K	$(S\text{-THBTD})_2CuCl_6$ at 100 K	$(S\text{-THBTD})_2CuCl_6$ at 400 K
Crystal system	Triclinic	Triclinic	Triclinic	Triclinic
Space group	$P1$	$P1$	$P1$	$P1$
Unit cell dimensions	$a = 7.9289(3)$ Å, $\alpha = 80.228(2)°$	$a = 7.9425(8)$ Å, $\alpha = 80.3380(10)°$	$a = 7.9251(6)$ Å, $\alpha = 81.219(2)°$	$a = 7.9476(10)$ Å, $\alpha = 79.779(7)°$
	$b = 8.7451(3)$ Å, $\beta = 88.9030(10)°$	$b = 8.6593(8)$ Å, $\beta = 88.8210(10)°$	$b = 8.5677(6)$ Å, $\beta = 88.198(2)°$	$b = 8.8059(12)$ Å, $\beta = 89.351(7)°$
	$c = 8.8198(3)$ Å, $\gamma = 87.605(2)°$	$c = 8.8291(9)$ Å, $\gamma = 87.3220(10)°$	$c = 8.7377(7)$ Å, $\gamma = 86.916(2)°$	$c = 8.8600(11)$ Å, $\gamma = 88.008(7)°$
Volume	$602.11(4)$ Å^3	$597.92(10)$ Å^3	$585.32(8)$ Å^3	$609.86(14)$ Å^3
Z	1	1	1	1
Independent reflections	$4308\ [R_{int} = 0.0258]$	$4339\ [R_{int} = 0.0217]$	$3970\ [R_{int} = 0.0362]$	$4245\ [R_{int} = 0.0445]$
Completeness to $\theta = 25.242°$	99.2%	99.9%	98.3%	99.3%
Refinement method	Full-matrix least-squares on F^2	Full-matrix least-squares on F^2	Full-matrix least-squares on F^2	Full-matrix least-squares on F^2
Data/restraints/parameters	4308/3/265	4339/3/265	3970/3/265	4245/3/265
Goodness-of-fit	1.014	1.070	1.055	1.056
Final R indices $[I > 2\sigma(I)]$	$R_{obs} = 0.0290$, $wR_{obs} = 0.0754$	$R_{obs} = 0.0217$, $wR_{obs} = 0.0625$	$R_{obs} = 0.0240$, $wR_{obs} = 0.0615$	$R_{obs} = 0.0339$, $wR_{obs} = 0.0954$
R indices [all data]	$R_{all} = 0.0327$, $wR_{all} = 0.0797$	$R_{all} = 0.0227$, $wR_{all} = 0.0633$	$R_{all} = 0.0241$, $wR_{all} = 0.0616$	$R_{all} = 0.0432$, $wR_{all} = 0.1005$
Largest diff. peak and hole	1.125 and -0.291 e·Å^{-3}	0.380 and -0.256 e·Å^{-3}	0.301 and -0.463 e·Å^{-3}	0.479 and -0.345 e·Å^{-3}

[a] $R = \Sigma||F_o| - |F_c||/\Sigma|F_o|$, $wR = \{\Sigma[w(|F_o|^2 - |F_c|^2)^2]/\Sigma[w(|F_o|^4)]\}^{1/2}$ and $w = 1/[\sigma^2(F_o^2) + (0.0247P)^2 + 0.3469P]$, where $P = (F_o^2 + 2F_c^2)/3$.
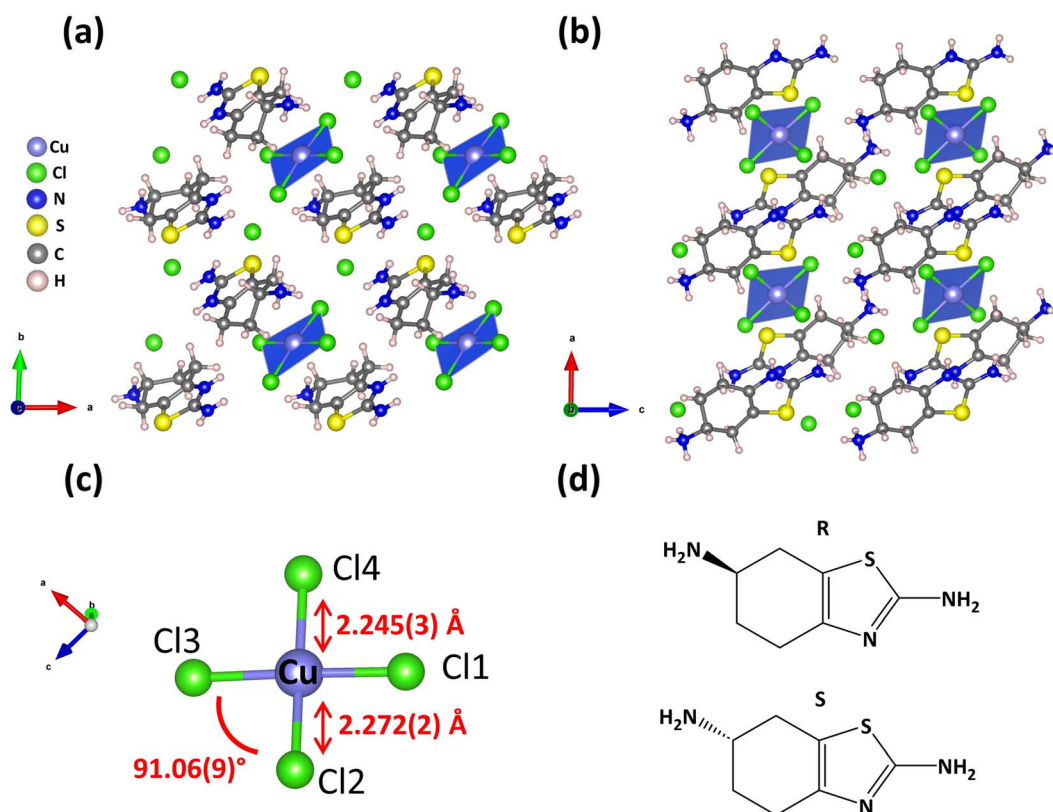

Fig. 1 Part of the crystal structure of $(R\text{-THBTD})_2CuCl_6$ viewed along the (a) c-axis and (b) b-axis, respectively. (c) Representation of the square planar geometry of the $[CuCl_4]^{2-}$ moieties along with two representative Cu–Cl bond lengths and one Cl–Cu–Cl angle. (d) The molecular structures of the chiral ligands S-THBTD and R-THBTD.

25732 | J. Mater. Chem. A, 2024, **12**, 25730–25739

This journal is © The Royal Society of Chemistry 2024

(R–NH$_3$), the aromatic primary amine (R–NH$_2$) and the aromatic secondary amine (–NH=), and the Cl atoms of the [CuCl$_4$]$^{2-}$ moieties. The corresponding bond distances (N–H⋯Cl) feature values spanning from 2.39 Å to 2.71 Å, signaling moderate to strong hydrogen bonding interactions (Fig. S3†). On the other hand, the out-of-plane hydrogen bonding interactions are much weaker, spanning from 3.14 to 3.37 Å, thus impacting to a much smaller extent the coordination geometry of Cu(II) ions.

The absence of symmetry elements dictates a triclinic $P1$ space group, which prompted us to explore whether there are underlying structural phase transitions that would lift the non-centrosymmetric nature.[32] Evidently, variable-temperature XRD studies at 100 K and 400 K revealed that the structure maintains its polar nature, as (S-THBTD)$_2$CuCl$_6$ crystallizes in the $P1$ space group in both cases (Table 1). This performance is quite uncommon for hybrid metal halide materials, which feature multiple phase transitions within the examined temperature range (100 K–400 K).[33] We observed only a gradual increase in the unit cell volume due to thermal expansion (from 585.32(8) Å^3 at 100 K to 609.86(14) Å^3 at 400 K).

In-house powder X-ray diffraction (PXRD) studies confirmed the uniform phase purity of the as-made crystals since experimental PXRD patterns and calculated ones from single crystal XRD studies are identical. Furthermore, (R-/S-THBTD)$_2$CuCl$_6$ have maintained their structural integrity in air for a year so far. After 12 months of air exposure, the experimental PXRD patterns of the air-treated materials are identical to those of the freshly made ones (Fig. 2 and S4†). There is no appearance of additional, unpredicted from the crystal structure diffraction peaks, indicative of structure degradation. Single crystal XRD studies of the 1 year air-treated (R-THBTD)$_2$CuCl$_6$ analog (Tables S17–21†) corroborate the above results. A comparison of the PXRD patterns for the 1 year air-treated (R-THBTD)$_2$CuCl$_6$ compound with the calculated pattern derived from the corresponding solved single-crystal structure reveals no changes (Fig. S5†), confirming phase purity. It is pointed out that this is record air stability performance for chiral magnetic MHSs.[30,34] We ascribe this to the 0D nature of the structure, where the [CuCl$_4$]$^{2-}$ moieties are shielded from incoming H$_2$O molecules due to the presence of the bulky, hydrophobic THBTD counter cations. In general, hybrid Cu halides exhibit improved air stability as compared to fully inorganic ones due to the presence of the organic part of the structure. For example, Rb$_2$CuCl$_3$ degrades within a day in moist air,[35] while (R/S-MBA)$_2$CuX$_4$ (X = Cl, Br) are air-stable for 1 month.[30] Degradation products include the formation of hydrates (*e.g.*, Rb$_2$CuCl$_4$·2H$_2$O). Therefore, any strategy aiming at enhancing the hydrophobic nature of the material will improve air/moisture stability.

Thermogravimetric analysis (TGA) revealed that (R-/S-THBTD)$_2$CuCl$_6$ are thermally stable up to 181 °C. There are two decomposition steps at ~181 °C and ~293 °C (Fig. S6a†). The first weight loss (~35%) corresponds to the decomposition of the organic part of the structure and HCl, while the second step (~65%) is ascribed to the decomposition of the inorganic metal halide.

The corresponding thermal stability behavior is consistent with other reported Cu(II) metal halides.[22,36,37] Moreover, differential scanning calorimetry (DSC) measurements support the absence of phase transitions in the 25–180 °C range, further corroborating the XRD studies (Fig. S6b†).

DFT studies

In order to elucidate the electronic structure of the new compounds, first-principles DFT calculations were performed (the details of the calculations are given in the ESI†). The optimized structural parameters are in good agreement with the corresponding experimental values. Specifically, for both R/S systems, the lattice parameters a are slightly elongated with values of 0.08%/0.12%, whereas the b and c parameters are shortened by −2.2%/−1.5% and −0.3%/−0.4%, respectively. Similarly, the angles α are enlarged by 0.7%/1.3%, whereas the angles β and γ are contracted by −1.3%/−1.3% and −1.1%/−0.6%, for R/S systems, respectively. The calculated Cu–Cl$_2$/Cu–Cl$_4$ bond lengths, as shown in Fig. 1c, are found to be 2.303 Å/2.293 Å, respectively, whereas the corresponding angle is found to be 91.38°.

The systems are shown to exhibit ferromagnetic-like characteristics at low temperatures based on magnetometry studies. We have calculated the electronic band structures for (R-/S-THBTD)$_2$CuCl$_6$, in the ferromagnetic state, as plotted in Fig. 3a
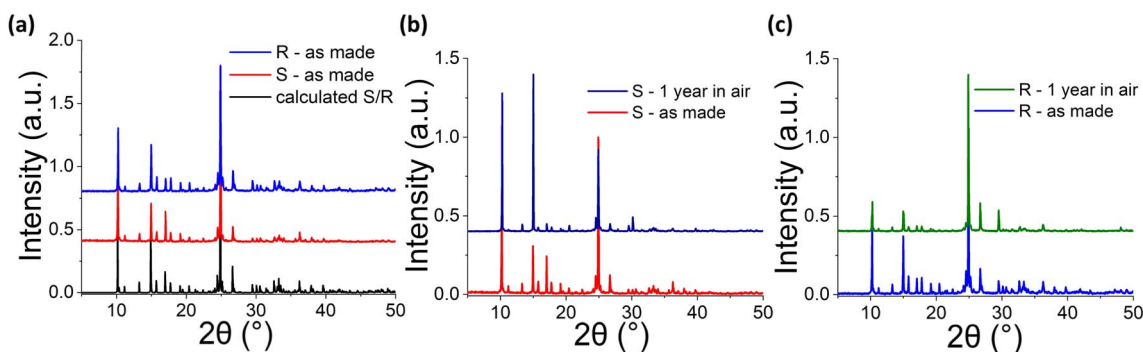

Fig. 2 (a) Comparison of the PXRD patterns for the as-made (R-/S-THBTD)$_2$CuCl$_6$ compounds to the calculated patterns derived from the solved single-crystal structure. (b) Comparison of the PXRD patterns for the S and (c) R enantiomers after 1 year of air exposure (RH = 35–55% ± 5%) to the calculated pattern derived from the solved single-crystal structure.
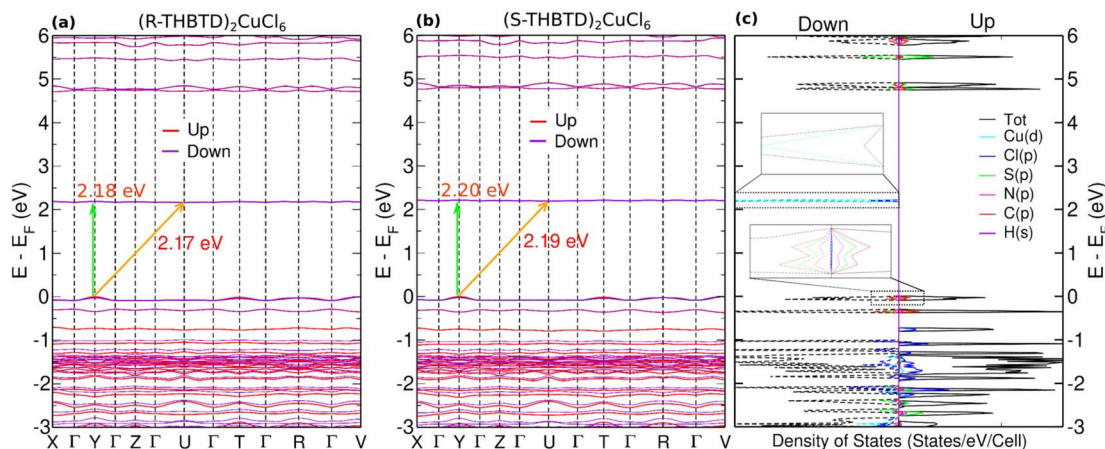
This journal is © The Royal Society of Chemistry 2024

J. Mater. Chem. A, 2024, **12**, 25730–25739 | **25733**

Fig. 3 Calculated band structures of the ferromagnetic phases of (a) (R-THBTD)$_2$CuCl$_6$ (b) and (S-THBTD)$_2$CuCl$_6$ materials, respectively. (c) Density of states of the (S-THBTD)$_2$CuCl$_6$ material, where the insets highlight an enlarged view of the PDOS that contributes to the VBM and CBM states. The spin-down and spin-up states are represented by a dashed line and a solid line, respectively.

and b. The highest valence band (VBM) for each system is slightly dispersed, whereas the lowest conduction band (CBM) is entirely flat, given the 0D nature of these systems. Both materials exhibit an indirect character for the fundamental band gap with values of 2.17 and 2.19 eV for (R-THBTD)$_2$CuCl$_6$ and (S-THBTD)$_2$CuCl$_6$, respectively. The corresponding band gap values feature a small difference of 0.02 eV and are in good agreement with the measured optical band gaps of the two materials, as discussed below. The direct transitions of the (R-/S-THBTD)$_2$CuCl$_6$ materials are found at the Y points of the Brillouin zone with values of 2.18 and 2.20 eV, for the R and S analogs, respectively, as shown in Fig. 3. Direct bandgap values lie at slightly higher energy than the indirect ones, closely matching the experimental trend from Tauc plot analysis (see the next section). It is pointed out that direct transitions from the highest valence band to the lowest conduction band may also occur in different regions of the Brillouin zone due to the flatness of the bands. The density of states (DOS) plotted in

Fig. 3c for the (S-THBTD)$_2$CuCl$_6$ system exhibits a sharp peak structure due to the zero dimensionality of the system. The partial density of states (PDOS) (and the band structures) show that both the spin-up and spin-down states contribute to the VBM, which is mainly dominated by the hybridization of the p orbitals of the C, N, and S atoms composing the organic molecule, whereas only the spin-down states contribute to the CBM that is primarily composed of the d and p orbitals of Cu and Cl elements.

Optical properties

Utilization of the Kubelka–Munk equation (see the ESI†) allowed the determination of the optical absorbance from UV-vis diffuse reflectance studies (Fig. S7†). The absorption spectra of (R-/S-THBTD)$_2$CuCl$_6$ display three major peaks, a narrow one at ∼285 nm which is associated with the π → π* transition of THBTD (Fig. S8†), a broad one at ∼390 nm which is attributed to

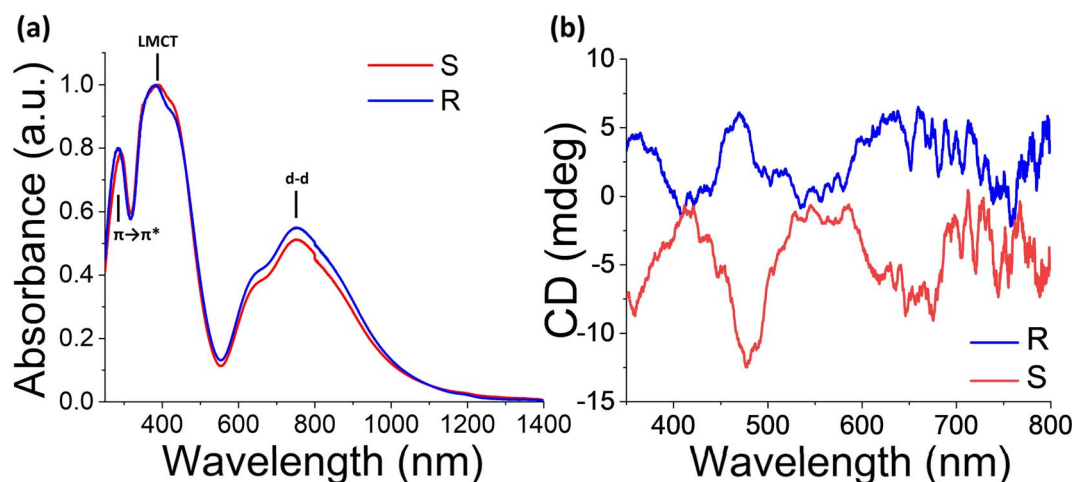**Fig. 4** (a) Comparison of normalized absorbance spectra for (R-THBTD)$_2$CuCl$_6$ and (S-THBTD)$_2$CuCl$_6$ along with the corresponding assigned transitions. (b) DRCD spectra for the (R-THBTD)$_2$CuCl$_6$ and (S-THBTD)$_2$CuCl$_6$ materials verifying their chiral nature.

25734 | J. Mater. Chem. A, 2024, **12**, 25730–25739

This journal is © The Royal Society of Chemistry 2024

the Cl to metal charge transfer (LMCT) and a broader vis-NIR at ~752 nm which can be attributed to Laporte forbidden Cu(II) d–d transitions (Fig. 4a).[28,31,38,39] Tauc plot analysis reveals both direct and indirect bandgaps associated with CT transitions. Apparently, for the indirect transition (Fig. S9c and d†), the corresponding bandgap values are 2.21 and 2.18 eV for the S and R analogs, while for the direct transition, the determined values are 2.53 and 2.50 eV for the S and R analogs, respectively (Fig. S9a and b†). The latter trend is consistent with the DFT band structure calculations. Prominently, both enantiomers show only miniscule changes in their optical absorption spectra after 1 year of air exposure, showcasing the robustness of the optical properties (Fig. S10†). The corresponding differences can be explained by examining closely the single crystal structure of the 1 year air-treated (R-/S-THBTD)$_2$CuCl$_6$ sample to the freshly prepared one. Apparently, the only noticeable difference is a slight elongation of the Cu–Cl bond lengths for the air-treated sample (see Table S22†), expanding from 2.247(2) and 2.272(2) Å to 2.2531(14) and 2.2761(17) Å for the fresh and air treated ones, respectively. This difference is potentially responsible for the miniscule shift in the corresponding LMCT peak in the UV-vis spectrum (Fig. S10a†) to higher energy values (from 2.88 eV to 2.93 eV), derived from the reduction in the Cu–Cl orbital overlap due to the bond elongation. In the same regard, the decrease in the relative intensity for the d–d transitions (1.65 eV) for the air-treated samples compared to the fresh ones is also ascribed to the increase in the distance of the Cl ligand from the metal center, thus inducing a decrease in the d–d transition probability.

Diffuse reflectance CD (DRCD) measurements on the as-made powder samples of (S-/R-THBTD)$_2$CuCl$_6$ reveal mirrored CD signals, confirming the non-centrosymmetric nature of the materials. The CD spectra of the two enantiomers feature multiple peaks at ~660, 470, and 360 nm, which are correlated to the CT and d–d transitions of the absorbance spectra. Completely different CD spectra for the hybrid semiconductors *versus* the chiral molecules S-THBTD and R-THBTD indicate that the corresponding CD signals do not derive from the states of the chiral organic cations.[40] For determining the anisotropy factor (g_{CD}), the following equation was utilized:

$$g_{CD|abs|} = \frac{CD_{(mdeg)}}{32980 \times A}$$

where A is the conventional absorbance of non-polarized light and CD is the differential absorbance of left and right circularly polarized lights, respectively. The maximum anisotropy factor of (S-THBTD)$_2$CuCl$_6$ and (R-THBTD)$_2$CuCl$_6$ turned out to be 6.8 × 10^{-4} and 2.8 × 10^{-4} at 478 nm and 471 nm, respectively. These values are one order of magnitude lower than those of 0D (R-/S-1,2-NEA)$_2$CuCl$_4$, and three orders of magnitude lower than those of 0D (R-MBA)$_2$CuCl$_4$ and (R-/S-1,1-NEA)$_2$CuCl$_4$.[31,41]

Magnetic properties

To characterize the magnetic properties of the samples, we evaluated the temperature-dependent magnetic susceptibility (χ). In Fig. 5a and c, the observed χ increases with decreasing temperature under a 0.1 T static magnetic field, as thermal fluctuations become less potent. It is worth noticing that χ
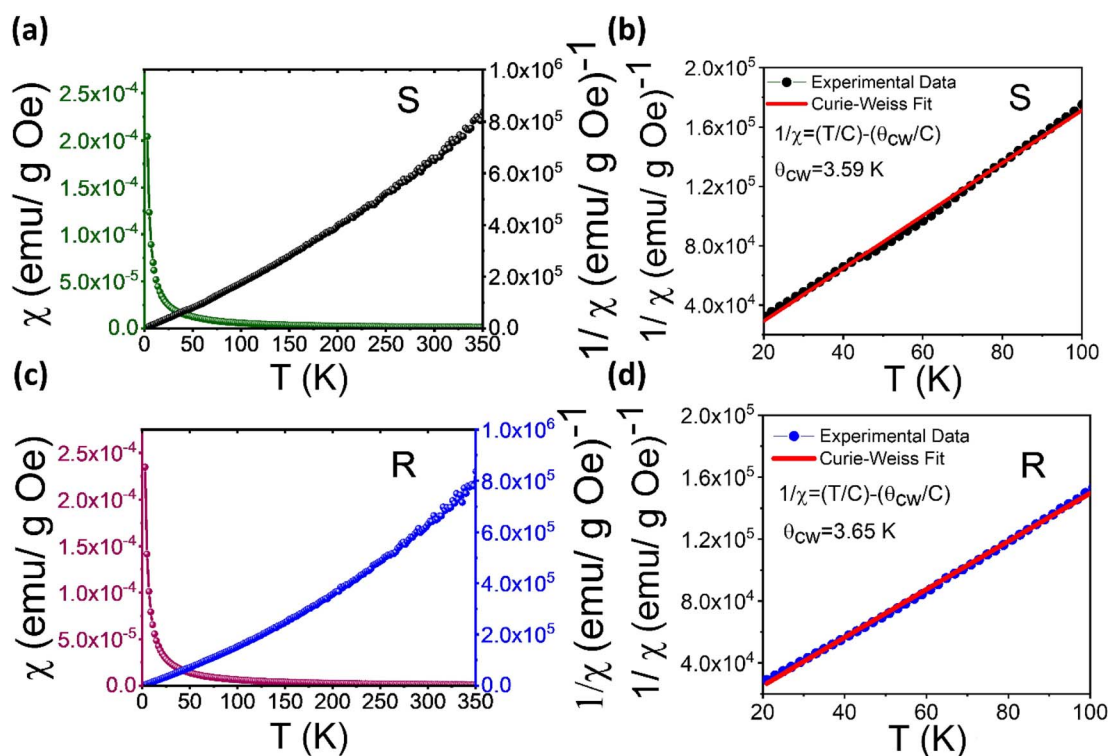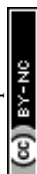

Fig. 5 Temperature-dependent magnetic susceptibility (χ) and inverse $1/\chi$ under a 0.1 T static magnetic field of (a) (S-THBTD)$_2$CuCl$_6$ and (c) (R-THBTD)$_2$CuCl$_6$; Curie–Weiss fit (red line) within the range of 20–100 K for (b) (S-THBTD)$_2$CuCl$_6$ and (d) (R-THBTD)$_2$CuCl$_6$, respectively.

This journal is © The Royal Society of Chemistry 2024

J. Mater. Chem. A, 2024, **12**, 25730–25739 | **25735**

increases sharply at temperatures below 6 K. This might imply that the material undergoes a transition from the paramagnetic (PM) to a ferromagnetic (FM)-like state below 6 K. The Curie–Weiss equation (shown in Fig. 5b and d), capturing the magnetic susceptibility of a material in the paramagnetic region, was utilized to fit the experimental data for the temperature-dependent inverse susceptibility (Fig. 5a and c). As shown in Fig. 5b and d, the fitting focused on the temperature range of 20 K to 100 K, revealing a linear behavior of χ with respect to change in temperature. It is noticed here that we have found a negligible effect of diamagnetic correction from ligands present in the samples on the fit of the temperature-dependent susceptibility data.

The Curie–Weiss temperatures (θ_{CW}) serve as approximate indicators of the strength of magnetic correlations between magnetic ions, with higher θ_{CW} values suggesting stronger magnetic correlations. The positive sign of θ_{CW} implies FM interactions, while its negative sign refers to antiferromagnetic (AFM) interactions at $T < \theta_{CW}$. The θ_{CW} values obtained from the fitting results (Fig. 5b and d) for $(S\text{-THBTD})_2CuCl_6$ and $(R\text{-THBTD})_2CuCl_6$ are 3.59 K and 3.65 K, respectively. The positive values of θ_{CW} seem to suggest the existence of FM-like couplings at $T < \theta_{CW}$. From the obtained fit parameters (Curie constant values, $C = 5.62 \times 10^{-4}$ emu K Oe^{-1} g^{-1} for $(S\text{-THBTD})_2CuCl_6$ and $C = 6.44 \times 10^{-4}$ emu K Oe^{-1} g^{-1} for $(R\text{-THBTD})_2CuCl_6$), the effective magnetic moment (μ_{eff}) values are also calculated to be 1.67 μ_B and 1.78 μ_B for $(S\text{-THBTD})_2CuCl_6$ and $(R\text{-THBTD})_2CuCl_6$, respectively, using the relationship: $\mu_{eff} = \sqrt{8C}\mu_B$ in cgs, where μ_B is the Bohr magneton.

We note that while the $\chi^{-1}(T)$ curve may not distinctly deviate from linearity due to the onset of FM-like ordering at low temperatures, the combination of the $\chi^{-1}(T)$ fit and field-dependent magnetization data suggests a deviation from purely paramagnetic behavior. Fig. 6a and b and 7a and b display the magnetic field-dependent magnetization (M–H) curves of the two samples at different temperatures. Notably, the M–H loops for temperatures below 6 K exhibit a subtle

alteration in shape, deviating from a typical paramagnetic behavior observed at higher temperatures for both samples (Fig. 6a and b). A similar behavior has recently been reported for $(R)\text{-(FE)}_2CuCl_4\text{-(1D)}$.[27] This suggests that as the applied external magnetic field increases, magnetic moments become more aligned with the magnetic field, giving rise to the total magnetic moment for both samples. A saturation trend in magnetization with respect to the magnetic field observed at low temperatures (<4 K) is of particular interest, as it might give hints at the occurrence of the PM–FM transition and the existence of structurally driven spin chirality in the presently investigated MHSs.

Following the method adopted in previous studies,[42,43] we have treated this weak ferromagnetism akin to ideal paramagnetism to estimate the saturation magnetization of our samples. Thus, the magnetic response at low temperatures (e.g., M–H at 2.3 K) can be modeled using the Brillouin function within the context of equations describing ferromagnetic ordering:

$$M = Ng_J J\mu_B \left[\frac{2J+1}{2J}\coth\left(\frac{2J+1}{2J}y\right) - \frac{1}{2J}\coth\left(\frac{y}{2J}\right) \right]$$

where $y = \dfrac{g_J J\mu_B H}{k_B T}$;

$H = H_{app} + H_{mol}$ (H_{app} is the applied magnetic field and H_{mol} is the Weiss molecular magnetic field); $N = \dfrac{M_s}{g_J\mu_B}$, where M_s is the saturation magnetization; g_J is the Lande' g-factor. It is evident in Fig. 6 that for both samples, the experimental data diverge from the Brillouin function fit anticipated for $S = 1/2$, indicating non-paramagnetic behavior at low temperatures (e.g., 2.3 K). The experimentally determined magnetic moment exceeds that derived from the Brillouin function fit, suggesting FM-like behavior in the samples at low temperatures. A similar phenomenon has been observed in cyclic dimer Ln_2L_2 complexes constructed from (3-pyridinylmethoxy)phenyl-substituted nitronyl nitroxide ligands, where the magnetic
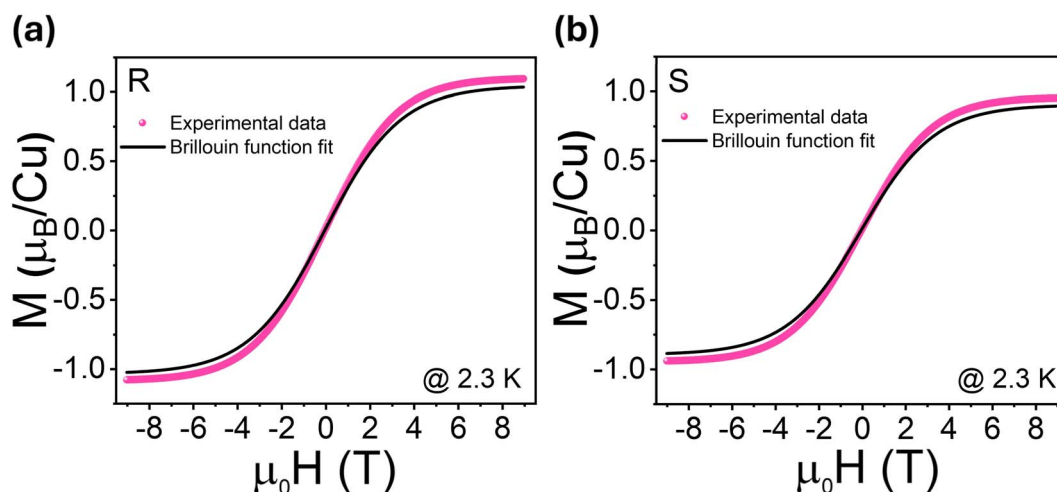
Fig. 6 The M–H data taken at 2.3 K for (a) $(R\text{-THBTD})_2CuCl_6$ and (b) $(S\text{-THBTD})_2CuCl_6$. The solid line (black) represents the Brillouin function for $S = 1/2$ ($g = 2.0$ and $T = 2.3$ K).

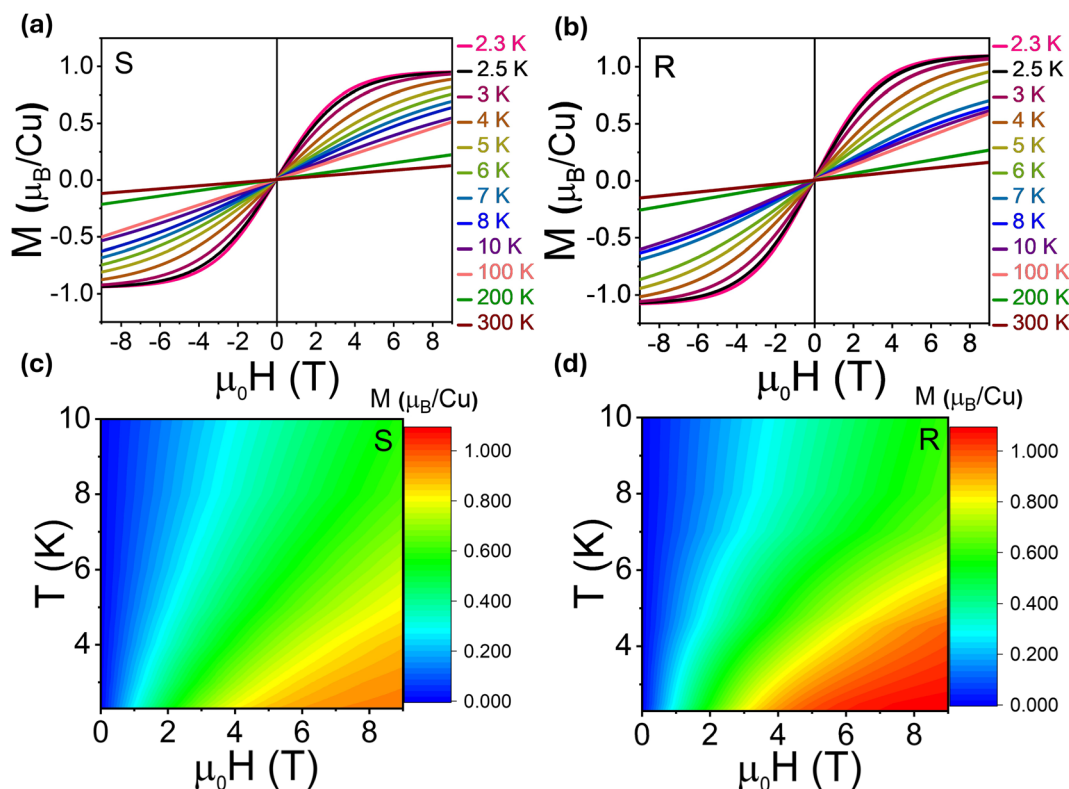**25736** | J. Mater. Chem. A, 2024, **12**, 25730–25739

This journal is © The Royal Society of Chemistry 2024

Fig. 7 Magnetic-field dependent magnetization (M−H) curves of (a) (S-THBTD)$_2$CuCl$_6$ and (b) (R-THBTD)$_2$CuCl$_6$ in a temperature range from 2.3 to 300 K; the 2D surface plots of change in magnetic moment with field and temperature for (c) (S-THBTD)$_2$CuCl$_6$ and (d) (R-THBTD)$_2$CuCl$_6$ for field changes up to 9 T and temperatures below 10 K.

moment value derived from the Brillouin function fit exceeds the experimental value, suggesting the presence of antiferromagnetic-like behavior.[43]

The low-temperature FM-like behavior of (S-THBTD)$_2$CuCl$_6$ and (R-THBTD)$_2$CuCl$_6$ has been further confirmed by the observation of a small magnetic hysteresis in the M−H curve at low temperature (e.g., 2.5 K), as shown in Fig. S12.† We have determined the coercive field (H_c) values from M−H measurements at temperatures below 6 K for (S-THBTD)$_2$CuCl$_6$. Our findings indicate a decrease in H_c from 2.4 mT at 2.5 K to 2.2 mT at 4 K, approaching 0 mT at 5 K, considering the uncertainty of the PPMS measurement. This observed trend in $H_c(T)$ strengthens our assertion that the material displays FM-like ordering at low temperatures.

From the M−H data, we also find that (R-THBTD)$_2$CuCl$_6$ possesses a greater magnetic moment ($\approx$ 9.86 emu g^{-1}) (at μ_0H = 9 T and at 2.3 K) as compared to (S-THBTD)$_2$CuCl$_6$ ($\approx$ 8.57 emu g^{-1}) (at μ_0H = 9 T and at 2.3 K). This is in good agreement with that obtained from the μ_{eff} calculations. These values correlate well to other Cu(II) based MHSs, such as (3ampy)CuCl$_4$ with 17.17 emu g^{-1},[44] (R-/S-MPEA)$_2$CuCl$_4$ with 12.5 emu g^{-1},[20] and (R-/S-)-(FE)$_2$CuCl$_4$ with 9.33 emu g^{-1}.[27]

To capture the interplay of magnetization, magnetic field and temperature, two-dimensional (2D) surface plots are displayed in Fig. 7c and d. Cool colors denote lower magnetic moment values, while warm colors signify higher values. It can

be seen that at the measured lowest temperature (2.3 K), the magnetic field at which the magnetization changes its slope is around 4 T for (S-THBTD)$_2$CuCl$_6$ (Fig. 7c), while it is considerably smaller, around 3 T, for (R-THBTD)$_2$CuCl$_6$ (Fig. 7d). This might suggest some correlation between the structure and magnetism in the MHS systems. Nevertheless, further studies are needed to confirm this in a concrete way.

To demonstrate that 1 year of air exposure had no impact on the magnetic properties of (R-THBTD)$_2$CuCl$_6$, magnetic field-dependent magnetization (M−H) studies were performed, revealing no change for the air-treated sample compared to the fresh one (Fig. S13† and 7b). The corresponding magnetic moment for the 1 year air-treated sample is 9.67 emu g^{-1} (at μ_0H = 9 T and 2.3 K), which correlates pretty well to the fresh sample's value of 9.86 emu g^{-1} (at μ_0H = 9 T and 2.3 K), validating the integrity of the magnetic properties.

Conclusions

Considering the importance of developing chiral magnetic MHSs and elucidating the underlying structure–property relationships, we synthesized two new polar 0D materials, namely (S-/R-THBTD)$_2$CuCl$_6$, and characterized their properties. Cu(II) cations feature an uncommon characteristic for MHSs, square planar geometry, imposed by multiple hydrogen bonds in-plane, while the structure maintains its non-centrosymmetric nature from 100 to 400 K based on single crystal XRD studies. Both analogs have

This journal is © The Royal Society of Chemistry 2024

J. Mater. Chem. A, 2024, **12**, 25730–25739 | **25737**

retained their structural integrity and magnetic and optical properties for a year so far, based on XRD, magnetometry and UV-vis studies, a record performance among chiral magnetic MHSs. DRCD measurements confirmed the chiral character of the two enantiomers, while magnetization studies revealed a saturation magnetization value of up to 9.86 emu g^{-1} at low temperatures (e.g., 2.3 K), among the highest reported for chiral magnetic MHSs. Our work demonstrates the versatility and immense potential of MHSs for demanding applications, where chirality, magnetism and stability are interwoven.

Data availability

The data supporting this article have been included as part of the ESI.†

Conflicts of interest

The authors declare no competing financial interest.

Acknowledgements

References

1 N. Gisin and R. Thew, Quantum communication, Nat. Photonics, 2007, 1, 165–171.

2 Y. Yang, R. C. da Costa, M. J. Fuchter and A. J. Campbell, Circularly polarized light detection by a chiral organic semiconductor transistor, Nat. Photonics, 2013, 7, 634–638.

3 T. Liu, X. Wang, H. Wang, G. Shi, F. Gao, H. Feng, H. Deng, L. Hu, E. Lochner, P. Schlottmann, S. von Molnár, Y. Li, J. Zhao and P. Xiong, Linear and Nonlinear Two-Terminal Spin-Valve Effect from Chirality-Induced Spin Selectivity, ACS Nano, 2020, 14, 15983–15991.

4 O. B. Dor, S. Yochelis, S. P. Mathew, R. Naaman and Y. Paltiel, A chiral-based magnetic memory device without a permanent magnet, Nat. Commun., 2013, 4, 2256.

5 Q. Liu, Q. Wei, H. Ren, L. Zhou, Y. Zhou, P. Wang, C. Wang, J. Yin and M. Li, Circular polarization-resolved ultraviolet photonic artificial synapse based on chiral perovskite, Nat. Commun., 2023, 14, 7179.

6 J. Ma, H. Wang and D. Li, Recent Progress of Chiral Perovskites: Materials, Synthesis, and Properties, Adv. Mater., 2021, 33, 2008785.

7 S. Ma, J. Ahn and J. Moon, Chiral Perovskites for Next-Generation Photonics: From Chirality Transfer to Chiroptical Activity, Adv. Mater., 2021, 33, 2005760.

8 P.-J. Huang, K. Taniguchi and H. Miyasaka, Bulk Photovoltaic Effect in a Pair of Chiral–Polar Layered Perovskite-Type Lead Iodides Altered by Chirality of Organic Cations, J. Am. Chem. Soc., 2019, 141, 14520–14523.

9 K. Wang, L. Qian, S.-C. Ying and G. Xiao, Spin–orbit torque switching of chiral magnetization across a synthetic antiferromagnet, Commun. Phys., 2021, 4, 10.

10 F. Fan, D. Zhao, Z. Tan, Y. Ji, J. Cheng and S. Chang, Magnetically Induced Terahertz Birefringence and Chirality Manipulation in Transverse-Magnetized Metasurface, Adv. Opt. Mater., 2021, 9, 2101097.

11 Q. Dong, Y. Fang, Y. Shao, P. Mulligan, J. Qiu, L. Cao and J. Huang, Electron–hole diffusion lengths >175 μm in solution-grown $CH_3NH_3PbI_3$ single crystals, Science, 2015, 347, 967–970.

12 S. D. Stranks, G. E. Eperon, G. Grancini, C. Menelaou, M. J. P. Alcocer, T. Leijtens, L. M. Herz, A. Petrozza and H. J. Snaith, Electron-Hole Diffusion Lengths Exceeding 1 Micrometer in an Organometal Trihalide Perovskite Absorber, Science, 2013, 342, 341–344.

13 C. Zhang, D. Sun, C. X. Sheng, Y. X. Zhai, K. Mielczarek, A. Zakhidov and Z. V. Vardeny, Magnetic field effects in hybrid perovskite devices, Nat. Phys., 2015, 11, 427–434.

14 M. Isarov, L. Z. Tan, M. I. Bodnarchuk, M. V. Kovalenko, A. M. Rappe and E. Lifshitz, Rashba Effect in a Single Colloidal $CsPbBr_3$ Perovskite Nanocrystal Detected by Magneto-Optical Measurements, Nano Lett., 2017, 17, 5020–5026.

15 M. Kepenekian and J. Even, Rashba and Dresselhaus Couplings in Halide Perovskites: Accomplishments and Opportunities for Spintronics and Spin–Orbitronics, J. Phys. Chem. Lett., 2017, 8, 3362–3370.

16 T. H. Moon, S.-J. Oh and K. M. Ok, $[((R)-C_8H_{12}N)_4][Bi_2Br_{10}]$ and $[((S)-C_8H_{12}N)_4][Bi_2Br_{10}]$: Chiral Hybrid Bismuth Bromides Templated by Chiral Organic Cations, ACS Omega, 2018, 3, 17895–17903.

17 K. Taniguchi, M. Nishio, N. Abe, P.-J. Huang, S. Kimura, T.-h. Arima and H. Miyasaka, Magneto-Electric Directional Anisotropy in Polar Soft Ferromagnets of Two-Dimensional Organic–Inorganic Hybrid Perovskites, Angew. Chem., Int. Ed., 2021, 60, 14350–14354.

18 H. Lu, T. He, H. Wu, F. Qi, H. Wang, B. Sun, T. Shao, T. Qiao, H.-L. Zhang, D. Sun, Y. Chen, Z. Tang and G. Long, Chiral Ruthenium Halide Semiconductor with Strong Antiferromagnetic Coupling, Adv. Funct. Mater., 2024, 34, 2308862.

19 L. Mao, J. Chen, P. Vishnoi and A. K. Cheetham, The Renaissance of Functional Hybrid Transition-Metal Halides, Acc. Mater. Res., 2022, 3, 439–448.

20 B. Sun, X.-F. Liu, X.-Y. Li, Y. Zhang, X. Shao, D. Yang and H.-L. Zhang, Two-Dimensional Perovskite Chiral Ferromagnets, Chem. Mater., 2020, 32, 8914–8920.

21 J. Xue, Z. Wang, A. Comstock, Z. Wang, H. H. Y. Sung, I. D. Williams, D. Sun, J. Liu and H. Lu, Chemical Control

25738 | J. Mater. Chem. A, 2024, 12, 25730–25739

This journal is © The Royal Society of Chemistry 2024

of Magnetic Ordering in Hybrid Fe–Cl Layered Double Perovskites, *Chem. Mater.*, 2022, **34**, 2813–2823.

22 D. P. Panda, D. Swain and A. Sundaresan, Photophysical and Magnetic Properties in Zero-Dimensional (H_2DABCO) $MX_4 \cdot nH_2O$ (M = Mn and Cu; X = Cl and Br; n = 0, 1, and 4), *J. Phys. Chem. C*, 2022, **126**, 13291–13299.

23 K. Taniguchi, P.-J. Huang, S. Kimura and H. Miyasaka, Chiral weak ferromagnets formed in one-dimensional organic–inorganic hybrid manganese chloride hydrates, *Dalton Trans.*, 2022, **51**, 17030–17034.

24 Y. Ai, R. Sun, W.-Q. Liao, X.-J. Song, Y.-Y. Tang, B.-W. Wang, Z.-M. Wang, S. Gao and R.-G. Xiong, Unprecedented Ferroelectricity and Ferromagnetism in a Cr^{2+}-Based Two-Dimensional Hybrid Perovskite, *Angew. Chem., Int. Ed.*, 2022, **61**, e202206034.

25 S.-P. Feng, Y. Cheng, H.-L. Yip, Y. Zhong, P. W. K. Fong, G. Li, A. Ng, C. Chen, L. A. Castriotta, F. Matteocci, L. Vesce, D. Saranin, A. D. Carlo, P. Wang, J. Wei Ho, Y. Hou, F. Lin, A. G. Aberle, Z. Song, Y. Yan, X. Chen, Y. Yang, A. A. Syed, I. Ahmad, T. Leung, Y. Wang, J. Lin, A. M. C. Ng, Y. Li, F. Ebadi, W. Tress, G. Richardson, C. Ge, H. Hu, M. Karimipour, F. Baumann, K. Tabah, C. Pereyra, S. R. Raga, H. Xie, M. Lira-Cantu, M. V. Khenkin, I. Visoly-Fisher, E. A. Katz, Y. Vaynzof, R. Vidal, G. Yu, H. Lin, S. Weng, S. Wang and A. B. Djurišić, Roadmap on commercialization of metal halide perovskite photovoltaics, *J. Phys.: Mater.*, 2023, **6**, 032501.

26 Z. Song, B. Yu, G. Liu, L. Meng and Y. Dang, Chiral Hybrid Copper(I) Iodide Single Crystals Enable Highly Selective Ultraviolet-Pumped Circularly Polarized Luminescence Applications, *J. Phys. Chem. Lett.*, 2022, **13**, 2567–2575.

27 H. Zheng, R. Zhang, X. Wu, Q. Zhang, Z. Wu, W. P. D. Wong, J. Chen, Q.-H. Xu and K. P. Loh, Strain-Driven Solid–Solid Crystal Conversion in Chiral Hybrid Pseudo-Perovskites with Paramagnetic-to-Ferromagnetic Transition, *J. Am. Chem. Soc.*, 2023, **145**, 3569–3576.

28 R. Das, D. Swain, A. Mahata, D. Prajapat, S. K. Upadhyay, S. Saikia, V. R. Reddy, F. De Angelis and D. D. Sarma, Family of Chiral Ferroelectric Compounds with Widely Tunable Band Gaps, *Chem. Mater.*, 2024, **36**, 1891–1898.

29 B. Li, Y. Yu, M. Xin, J. Xu, T. Zhao, H. Kang, G. Xing, P. Zhao, T. Zhang and S. Jiang, Second-order nonlinear optical properties of copper-based hybrid organic–inorganic perovskites induced by chiral amines, *Nanoscale*, 2023, **15**, 1595–1601.

30 Y. Lu, Q. Wang, R. He, F. Zhou, X. Yang, D. Wang, H. Cao, W. He, F. Pan, Z. Yang and C. Song, Highly Efficient Spin-Filtering Transport in Chiral Hybrid Copper Halides, *Angew. Chem., Int. Ed.*, 2021, **60**, 23578–23583.

31 J. Hao, H. Lu, L. Mao, X. Chen, M. C. Beard and J. L. Blackburn, Direct Detection of Circularly Polarized Light Using Chiral Copper Chloride–Carbon Nanotube Heterostructures, *ACS Nano*, 2021, **15**, 7608–7617.

32 Y. Xie, R. Song, A. Singh, M. K. Jana, V. Blum and D. B. Mitzi, Kinetically Controlled Structural Transitions in Layered Halide-Based Perovskites: An Approach to Modulate Spin Splitting, *J. Am. Chem. Soc.*, 2022, **144**, 15223–15235.

33 S. A. Cuthriell, C. D. Malliakas, M. G. Kanatzidis and R. D. Schaller, Cyclic versus Linear Alkylammonium Cations: Preventing Phase Transitions at Operational Temperatures in 2D Perovskites, *J. Am. Chem. Soc.*, 2023, **145**, 11710–11716.

34 T. M. McWhorter, Z. Zhang, T. D. Creason, L. Thomas, M.-H. Du and B. Saparov, $(C_7H_{11}N_2)_2MBr_4$ (M = Cu, Zn): X-Ray Sensitive 0D Hybrid Metal Halides with Tunable Broadband Emission, *Eur. J. Inorg. Chem.*, 2022, e202100954.

35 T. D. Creason, A. Yangui, R. Roccanova, A. Strom, M.-H. Du and B. Saparov, Rb_2CuX_3 (X = Cl, Br): 1D All-Inorganic Copper Halides with Ultrabright Blue Emission and Up-Conversion Photoluminescence, *Adv. Opt. Mater.*, 2020, **8**, 1901338.

36 C. Han, A. J. Bradford, J. A. McNulty, W. Zhang, P. S. Halasyamani, A. M. Z. Slawin, F. D. Morrison, S. L. Lee and P. Lightfoot, Polarity and Ferromagnetism in Two-Dimensional Hybrid Copper Perovskites with Chlorinated Aromatic Spacers, *Chem. Mater.*, 2022, **34**, 2458–2467.

37 C. Han, A. J. Bradford, A. M. Z. Slawin, B. E. Bode, E. Fusco, S. L. Lee, C. C. Tang and P. Lightfoot, Structural Features in Some Layered Hybrid Copper Chloride Perovskites: $ACuCl_4$ or A_2CuCl_4, *Inorg. Chem.*, 2021, **60**, 11014–11024.

38 R. Das, M. Hossain, A. Mahata, D. Swain, F. De Angelis, P. K. Santra and D. D. Sarma, Unique Chiro-optical Properties of the Weakly-2D (R-/S-MBA)$_2$CuBr$_4$ Hybrid Material, *ACS Mater. Lett.*, 2023, **5**, 1556–1564.

39 D. Cortecchia, H. A. Dewi, J. Yin, A. Bruno, S. Chen, T. Baikie, P. P. Boix, M. Grätzel, S. Mhaisalkar, C. Soci and N. Mathews, Lead-Free $MA_2CuCl_xBr_{4-x}$ Hybrid Perovskites, *Inorg. Chem.*, 2016, **55**, 1044–1052.

40 A. Azmy, D. M. Konovalova, L. Lepore, A. Fyffe, D. Kim, L. Wojtas, Q. Tu, M. T. Trinh, N. Zibouche and I. Spanopoulos, Synthesis and Optical Properties of One Year Air-Stable Chiral Sb(III) Halide Semiconductors, *Inorg. Chem.*, 2023, **62**, 20142–20152.

41 Z. Guo, J. Li, J. Liang, C. Wang, X. Zhu and T. He, Regulating Optical Activity and Anisotropic Second-Harmonic Generation in Zero-Dimensional Hybrid Copper Halides, *Nano Lett.*, 2022, **22**, 846–852.

42 N. Pathak, S. K. Gupta, C. L. Prajapat, S. K. Sharma, P. S. Ghosh, B. Kanrar, P. K. Pujari and R. M. Kadam, Defect induced ferromagnetism in MgO and its exceptional enhancement upon thermal annealing: a case of transformation of various defect states, *Phys. Chem. Chem. Phys.*, 2017, **19**, 11975–11989.

43 M. Zhu, Y. Li, L. Jia, L. Zhang and W. Zhang, Syntheses, crystal structures, and magnetic properties of cyclic dimer Ln_2L_2 complexes constructed from (3-pyridinylmethoxy)phenyl-substituted nitronyl nitroxide ligands, *RSC Adv.*, 2017, **7**, 36895–36901.

44 B. Sun, Z. Yan, Y. Cao, S. Ding, R. Li, B. Ma, X.-Y. Li, H. Yang, W. Yin, Y. Zhang, Q. Wang, X. Shao, D. Yang, D. Xue and H.-L. Zhang, Intrinsic Ferromagnetic Semiconductors with High Saturation Magnetization from Hybrid Perovskites, *Adv. Mater.*, 2023, **35**, 2303945.

This journal is © The Royal Society of Chemistry 2024

J. Mater. Chem. A, 2024, **12**, 25730–25739 | **25739**